IMPROVED INCOMPRESSIBLE SPH METHOD FOR NATURAL-CONVECTION FROM HEATED T-OPEN PIPE OF Al_2O_3-WATER NANOFLUID IN A CAVITY: Buongiorno's Two-Phase Model

by

Abdelraheem M. ALY [a,b*] ***and Sameh E. AHMED*** [a,b]

[a] Department of Mathematics, College of Science Abha, King Khalid University, Aba, Saudi Arabia
[b] Department of Mathematics, Faculty of Science, South Valley University, Qena, Egypt

Original scientific paper
https://doi.org/10.2298/TSCI201122148A

The unsteady natural-convection of Al_2O_3-water nanofluid form heated open T-pipe inside a cavity has been investigated by incompressible smoothed particle hydrodynamic (ISPH) method using non-homogenous two-phase Buongiorno's model. Different lengths and heights of T-pipe shape are considered. The side walls of the cavity are kept at cool temperature T_c and the horizontal walls are thermally insulated. The Lagrangian description of the controlling governing equations is discretized and solved using improved ISPH method. In this study, ISPH method is improved using kernel renormalization function for boundary treatment plus modification in the source term of pressure Poisson equation. The source term of pressure Poisson equation contains the velocity divergence plus density invariance multiply by relaxation coefficient. The calculations are performed for variable lengths of T-open pipe ($0.2 \le L_b \le 0.6$), variable widths of T-open pipe ($0.02 \le W_b \le 0.16$), ($0.02 \le W_t \le 0.16$), and variable concentration of nanoparticles volume fraction ($1\% \le \varphi_{avg} \le 10\%$). The obtained results showed that the maximum values of the stream function are reduced by 80.8% when φ_{avg} is increased from 1-10%. Additionally, as lengths and widths of the T-pipe are raised, the average Nusselt numbers at the vertical walls are enhanced.

Key words*: Buongiorno model, improved ISPH, nanofluid, natural-convection, square cavity, T-open pipe*

Introduction

There are several applications from studying natural-convection in closed cavities. The applications are cooling of the electronically devices, humidification and heat exchangers. In addition, the nanofluid has many uses and contributions in the industry of the cooling systems of engines, fridges and electronics, nuclear plants, solar collectors [1, 2], solar energy [3-5], petroleum industries and lubricants and seals [6]. Mahian *et al*. [7, 8] introduced fundamental and applications review parts for the modelling and simulations of nanofluid-flows. Rashidi *et al*. [7] summarized the impacts of the nanofluid on the performance of the condensing and evaporating systems. Rashidi *et al*. [9] introduced an additional review on the improvement of heat transfer using combinations between nanofluid and inserts. In the literature, there are two different models for simulation the nanofluid-flows, namely single and two-phase models. In the first model, namely single phase model, the fluid and nanoparticles are in thermal equilibrium [10-14]. In experimental studies [15], they reported that the enhancement on heat

* Corresponding author, e-mail: abdelreheam.abdallah@sci.svu.edu.eg

transfer by nanofluids was significant in the entrance region and the classical Shah equation cannot predict heat transfer of nanofluids. In the second model, namely two-phase model, the influences of the Brownian motion, thermophoresis and other interactions between the base fluid and nanoparticles are considered [16, 17]. Buongiorno [18] introduced the non-homogenous model for nanofluids by considering the impacts of Brownian, diffusion and thermophoresis. After Buongiorno, there are numerous studies focused on the two-phase model of the nanofluids [19-27]. Dogonchi *et al*. [28] studied the natural-convection in a porous gap filled with nanofluid below magnetic field effects. Dogonchi *et al*. [29] used CVFEM to study the impacts of a magnetic field on natural-convection of nanofluid in a wavy cavity. Rehman *et al*. [30] studied heat transfer from evenly heated *T*-shaped blade inside a trapezium enclosure. Sheikhzadeh *et al*. [31] compared between the homogenous and non-homogenous models of the nanofluids. Moltlagh and Soltanipour [32] introduced non-homogenous two-phase Buongiorno's model of Al_2O_3-water nanofluid inside an inclined cavity. Moltlagh *et a*l. [33] used two-phase model for Fe_3O_4-water nanofluid in an inclined porous semi-annulus. In their studies, the impacts of the nanoparticles diffusion were considered according to the Buongiorno's model. The SPH method was originally introduced by [34, 35]. Later, SPH method and its incompressible version entitled ISPH have been received several attentions in the several fields [36-47].

Taking into account all the previous works, it is found that the authors focused on the homogeneous models of the nanofluid (one-phase model or two-phase model). Also, the authors considered regular fluid domains. However, the non-homogeneous nanofluid model within complex geometries is not presented. Therefore, the main objective of this study is to examine the flow and thermal fields within an enclosure that is heated from inside by an open *T*-shaped pipe and is filled by nanofluids. The non-homogenous two-phase Buongiorno's model is applied to simulate the nanofluid case. The non-dimensional governing equations are solved numerically using the SPH method. The main outcomes revealed that distributions of the nanofluid temperature, the average Nusselt number along the inner boundaries and the average Nusselt number at the left wall are supported as widths of the *T*-pipe channels is increased.

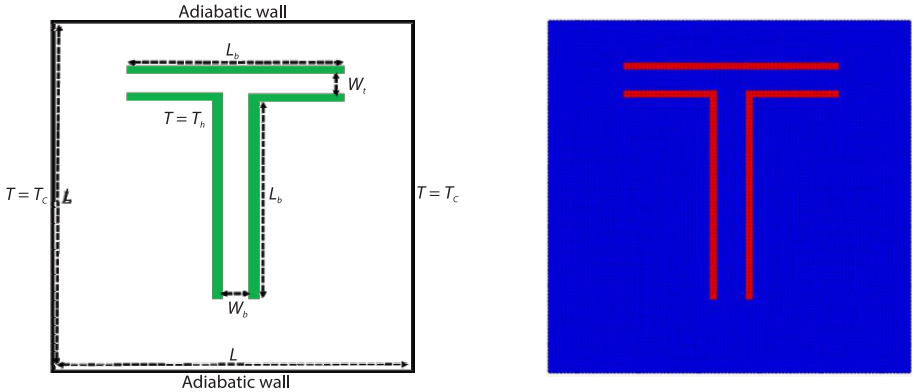

Figure 1. Initial schematic and particles model of *T*-open pipe inside a cavity

Mathematical formulations

Consider an unsteady, 2-D and laminar flow of an incompressible (constant density) nanofluid inside a square enclosure as depicted in fig. 1. The mentioned figure consists of a *T*-shaped open pipe within a square enclosure. Length of the outer boundary is L while the length of the inner *T*-pipe channels is denoted by L_b. Channels of the *T*-shaped pipe have width

W_b and W_t. The vertical walls of the enclosure have a relatively low temperature, T_c, while the horizontal walls are thermally insulated. The temperature differences inside the geometry are due to the uniform temperature condition $T_h(T_h \gg T_c)$ on the inner T-pipe. Uniformly shapes and equally sizes for the nanoparticles are assumed while the boundary conditions for the nanoparticles volume fractions at the vertical walls are zero mass fluxes. Variations of the density with the temperature are determined using the Boussinesq's approximation. The gravity acceleration is taken in the normal direction. The viscous dissipation and radiation impacts are neglected. The thermal equilibrium model between the base fluid and the nanoparticles is considered and the thermophysical properties of the base fluid and the nanoparticles volume fraction at 310 K are included in tab. 1. Under all these assumptions, the partial controlling equations in Lagrangian form are described [19]:

$$\frac{\partial u}{\partial x}+\frac{\partial v}{\partial y}=0 \tag{1}$$

$$\rho_{\mathrm{nf}}\frac{\mathrm{d}u}{\mathrm{d}t}=-\frac{\partial p}{\partial x}+\frac{\partial}{\partial x}\left(\mu_{\mathrm{nf}}\frac{\partial u}{\partial x}\right)+\frac{\partial}{\partial y}\left(\mu_{\mathrm{nf}}\frac{\partial u}{\partial y}\right) \tag{2}$$

$$\rho_{\mathrm{nf}}\frac{\mathrm{d}v}{\mathrm{d}t}=-\frac{\partial p}{\partial y}+\frac{\partial}{\partial x}\left(\mu_{\mathrm{nf}}\frac{\partial v}{\partial x}\right)+\frac{\partial}{\partial y}\left(\mu_{\mathrm{nf}}\frac{\partial v}{\partial y}\right)+\left(\rho\beta\right)_{\mathrm{nf}}\mathrm{g}\left(T-T_{\mathrm{c}}\right) \tag{3}$$

$$\left(\rho C_p\right)_{\mathrm{nf}}\frac{\mathrm{d}T}{\mathrm{d}t}=\nabla\left(k_{\mathrm{nf}}\nabla T\right)+C_{p,\mathrm{p}}\left[\rho_{\mathrm{p}}D_B\nabla\varphi+\frac{\rho_{\mathrm{p}}D_T}{T}\nabla T\right]\nabla T \tag{4}$$

$$\rho_{\mathrm{p}}\frac{\mathrm{d}\varphi}{\mathrm{d}t}=\nabla\left[\rho_p D_B\nabla\varphi+\frac{\rho_{\mathrm{p}}D_T}{T}\nabla T\right] \tag{5}$$

Table 1. Thermophysical properties of water and nanoparticles at 310 K

	ρ [kgm^{-3}]	K [Wm^{-1}K^{-1}]	C_p [Jkg^{-1}K^{-1}]	$\beta \cdot 10^{-5}$K^{-1}
Al_2O_3	3970	40	765	0.85
H_2O	993	0.628	4178	36.2

In the aforementioned system, D_B is the Brownian diffusion coefficient and it is expressed:

$$D_B=\frac{K_B T}{3\pi\mu_{\mathrm{f}}d_{\mathrm{p}}} \tag{6}$$

where $K_B = 1.380648 \cdot 10^{-23}$ J/K is the Boltzmann's constant, $\mu_f = 695 \cdot 10^{-6}$ kg/ms – the dynamic viscosity of water, and $d_p = 33$ nm is the diameter of the alumina molecule. In addition, D_T refers to the thermophoresis coefficient that is given:

$$D_T=0.26\frac{k_{\mathrm{f}}}{2k_{\mathrm{f}}+k_{\mathrm{p}}}\frac{\mu_{\mathrm{f}}}{\rho_{\mathrm{f}}T}\varphi \tag{7}$$

Further, the thermophysical properties of the nanofluid are assumed to be functions in the nanoparticle volume fraction and the diameters of H_2O and Al_2O_3 molecules, d_f and d_p based on the experimental results of Corcione [48], those are expressed:

$$\rho_{\mathrm{nf}}=\left(1-\varphi\right)\rho_{\mathrm{f}}+\varphi\rho_{\mathrm{p}} \tag{8}$$

$$\alpha_{\mathrm{nf}} = \frac{k_{\mathrm{nf}}}{\left(\rho C_p\right)_{\mathrm{nf}}} \tag{9}$$

$$\left(\rho C_p\right)_{\mathrm{nf}} = (1-\varphi)\left(\rho C_p\right)_{\mathrm{f}} + \varphi\left(\rho C_p\right)_{\mathrm{p}} \tag{10}$$

$$\left(\rho\beta\right)_{\mathrm{nf}} = (1-\varphi)\left(\rho\beta\right)_{\mathrm{f}} + \varphi\left(\rho\beta\right)_{\mathrm{p}} \tag{11}$$

$$\mu_{\mathrm{nf}} = \frac{\mu_{\mathrm{f}}}{\left[1-34.87\left(\frac{d_{\mathrm{p}}}{d_{\mathrm{f}}}\right)^{-0.3}\varphi^{1.03}\right]} \tag{12}$$

$$k_{\mathrm{nf}} = k_{\mathrm{f}}\left[1+4.4\left(\mathrm{Re}_B\right)^{0.4}\mathrm{Pr}^{0.66}\left(\frac{T}{T_{\mathrm{fr}}}\right)^{10}\left(\frac{k_{\mathrm{p}}}{k_{\mathrm{f}}}\right)^{0.03}\varphi^{0.66}\right] \tag{13}$$

$$\mathrm{Re}_B = \frac{\rho_{\mathrm{f}} u_B d_{\mathrm{p}}}{\mu_{\mathrm{f}}} \tag{14}$$

$$u_B = \frac{2K_B T}{\pi\mu_{\mathrm{f}} d_{\mathrm{p}}^2} \tag{15}$$

where T_{fr} is the freezing point of the base fluid and u_B – the Brownian velocity. Here, the values of d_{f} is assumed to be 0.385 nm.

The following dimensionless quantities are introduced:

$$X = \frac{x}{L},\ Y = \frac{y}{L},\ \tau = \frac{t\alpha_{\mathrm{f}}}{L^2},\ U = \frac{uL}{\alpha_{\mathrm{f}}},\ \alpha_f = \frac{k_{\mathrm{f}}}{\left(\rho C_p\right)_{\mathrm{f}}}$$

$$V = \frac{vL}{\alpha_{\mathrm{f}}},\ P = \frac{pL^2}{\rho_{\mathrm{nf}}\alpha_{\mathrm{f}}^2},\ \theta = \frac{T-T_{\mathrm{c}}}{T_{\mathrm{h}}-T_{\mathrm{c}}},\ \varphi^* = \frac{\varphi}{\varphi_{\mathrm{avg}}},\ D_B^* = \frac{D_B}{D_{Bo}},\ D_T^* = \frac{D_T}{D_{To}} \tag{16}$$

$$\delta = \frac{T_{\mathrm{c}}}{T_{\mathrm{h}}-T_{\mathrm{c}}},\ \mathrm{Ra} = \frac{\mathrm{g}\beta_{\mathrm{f}}\left(T_{\mathrm{h}}-T_{\mathrm{c}}\right)L^3}{\alpha_{\mathrm{f}}\nu_{\mathrm{f}}},\ \mathrm{Pr} = \frac{\nu_{\mathrm{f}}}{\alpha_{\mathrm{f}}},\ D_{To} = \gamma\frac{\mu_{\mathrm{f}}}{\rho_{\mathrm{f}}}\varphi_{\mathrm{avg}},\ D_{B0} = \frac{K_B T_c}{3\pi\mu_{\mathrm{f}} d_{\mathrm{p}}}$$

Then, the partial governing equations in Lagrangian and dimensionless forms are:

$$\frac{\partial U}{\partial X} + \frac{\partial V}{\partial Y} = 0 \tag{17}$$

$$\frac{\rho_{\mathrm{nf}}}{\rho_{\mathrm{f}}}\frac{\mathrm{d}U}{\mathrm{d}\tau} = -\frac{\rho_{\mathrm{nf}}}{\rho_{\mathrm{f}}}\frac{\partial P}{\partial X} + \frac{\partial}{\partial X}\left(\mathrm{Pr}\frac{\mu_{\mathrm{nf}}}{\mu_{\mathrm{f}}}\frac{\partial U}{\partial X}\right) + \frac{\partial}{\partial Y}\left(\mathrm{Pr}\frac{\mu_{\mathrm{nf}}}{\mu_{\mathrm{f}}}\frac{\partial U}{\partial Y}\right) \tag{18}$$

$$\frac{\rho_{\mathrm{nf}}}{\rho_{\mathrm{f}}}\frac{\mathrm{d}V}{\mathrm{d}\tau} = -\frac{\rho_{\mathrm{nf}}}{\rho_{\mathrm{f}}}\frac{\partial P}{\partial Y} + \frac{\partial}{\partial X}\left(\mathrm{Pr}\frac{\mu_{\mathrm{nf}}}{\mu_{\mathrm{f}}}\frac{\partial V}{\partial X}\right) + \frac{\partial}{\partial Y}\left(\mathrm{Pr}\frac{\mu_{\mathrm{nf}}}{\mu_{\mathrm{f}}}\frac{\partial V}{\partial Y}\right) + \frac{\left(\rho\beta\right)_{\mathrm{nf}}}{\left(\rho\beta\right)_{\mathrm{f}}}\mathrm{PrRa}\theta \tag{19}$$

$$\frac{\left(\rho C_p\right)_{\mathrm{nf}}}{\left(\rho C_p\right)_{\mathrm{f}}}\frac{\mathrm{d}\theta}{\mathrm{d}\tau}=\frac{\partial}{\partial X}\left(\frac{K_{\mathrm{nf}}}{K_{\mathrm{f}}}\frac{\partial\theta}{\partial X}\right)+\frac{\partial}{\partial Y}\left(\frac{K_{\mathrm{nf}}}{K_{\mathrm{f}}}\frac{\partial\theta}{\partial Y}\right)+$$
$$+\frac{1}{\mathrm{Le}}\left\{D_B^*\left[\frac{\partial\varphi^*}{\partial X}\frac{\partial\theta}{\partial X}+\frac{\partial\varphi^*}{\partial Y}\frac{\partial\theta}{\partial Y}\right]+\frac{D_T^*}{N_{BT}}\frac{\left[\left(\frac{\partial\theta}{\partial X}\right)^2+\left(\frac{\partial\theta}{\partial Y}\right)^2\right]}{1+\frac{\theta}{\delta}}\right\} \tag{20}$$

$$\frac{\mathrm{d}\varphi^*}{\mathrm{d}\tau}=\frac{\mathrm{Pr}}{\mathrm{Sc}}\frac{\partial}{\partial X}\left(D_B^*\frac{\partial\varphi^*}{\partial X}\right)+\frac{\mathrm{Pr}}{\mathrm{Sc}}\frac{\partial}{\partial Y}\left(D_B^*\frac{\partial\varphi^*}{\partial Y}\right)+$$
$$+\frac{\mathrm{Pr}}{\mathrm{Sc}}\frac{\partial}{\partial X}\left[\frac{D_T^*}{N_{BT}\left(1+\frac{\theta}{\delta}\right)}\frac{\partial\theta}{\partial X}\right]+\frac{\mathrm{Pr}}{\mathrm{Sc}}\frac{\partial}{\partial Y}\left[\frac{D_T^*}{N_{BT}\left(1+\frac{\theta}{\delta}\right)}\frac{\partial\theta}{\partial Y}\right] \tag{21}$$

where

$$\mathrm{Sc}=\frac{\nu_{\mathrm{f}}}{D_{B0}},\ \mathrm{Le}=\frac{K_{\mathrm{f}}}{\rho_{\mathrm{p}}C_{p,\mathrm{p}}\varphi_{\mathrm{avg}}D_{B0}},\ N_{BT}=\frac{\varphi_{\mathrm{avg}}D_{B0}T_c}{D_{T0}\left(T_{\mathrm{h}}-T_{\mathrm{c}}\right)}$$

are the Schmidt number, Lewis number, and the diffusivity ratio parameter, respetctively.

$$\text{On the side-walls, } U=0,\ V=0,\ \theta=0,\ \frac{\partial\varphi^*}{\partial X}=-\frac{D_T^*}{D_B^*}\frac{1}{N_{BT}}\frac{\frac{\partial\theta}{\partial X}}{1+\frac{\theta}{\delta}}$$

$$\text{On the horizontal-walls, } U=0,\ V=0,\ \frac{\partial\varphi^*}{\partial Y}=0,\ \frac{\partial\theta}{\partial Y}=0$$

$$\text{On te inner } T\text{-pipe shape, } \theta=1,\ \frac{\partial\varphi^*}{\partial n}=-\frac{D_T^*}{D_B^*}\frac{1}{N_{BT}}\frac{\frac{\partial\theta}{\partial n}}{1+\frac{\theta}{\delta}} \tag{22}$$

The local and average Nusselt numbers are defined:

$$\text{On the inner } T\text{-pipe: } \overline{\mathrm{Nu}}=-\frac{K_{\mathrm{nf}}}{k_{\mathrm{f}}}\frac{1}{S}\int_0^S\frac{\partial\theta}{\partial\boldsymbol{n}}\mathrm{d}S \tag{23}$$

$$\overline{\mathrm{Nu}}=-\frac{K_{\mathrm{nf}}}{k_{\mathrm{f}}}\int_0^L\frac{\partial\theta}{\partial X}\Big|_{X=0}\mathrm{d}Y \tag{24}$$

where S is the total interior shape length and $\boldsymbol{n}$ – the normal vector.

The ISPH method

In this section, the solving technique of the partial controlling equations with formulation of ISPH method were discussed in details.

First, projection scheme [49] is used as a solving technique for the non-dimensional forms: Initially, the intermediate velocities will be calculated:

$$U^* = U^n + \Delta\tau \mathrm{Pr}\frac{\rho_\mathrm{f}}{\rho_\mathrm{nf}}\left[\frac{\partial}{\partial X}\left(\frac{\mu_\mathrm{nf}}{\mu_\mathrm{f}}\frac{\partial U}{\partial X}\right)^n + \frac{\partial}{\partial Y}\left(\frac{\mu_\mathrm{nf}}{\mu_\mathrm{f}}\frac{\partial U}{\partial Y}\right)^n\right] \tag{25}$$

$$V^* = V^n + \Delta\tau \mathrm{Pr}\frac{\rho_\mathrm{f}}{\rho_\mathrm{nf}}\left[\frac{\partial}{\partial X}\left(\frac{\mu_\mathrm{nf}}{\mu_\mathrm{f}}\frac{\partial V}{\partial X}\right)^n + \frac{\partial}{\partial Y}\left(\frac{\mu_\mathrm{nf}}{\mu_f}\frac{\partial V}{\partial Y}\right)^n + \frac{(\rho\beta)_\mathrm{nf}}{(\rho\beta)_\mathrm{f}}\mathrm{Ra}\theta^n\right] \tag{26}$$

The pressure Poisson equation (PPE):

$$\nabla^2 P^{n+1} = \frac{1}{\rho_\mathrm{nf}}\frac{1}{\Delta\tau}\left[\frac{\partial\left(\rho_\mathrm{nf}U^*\right)}{\partial X} + \frac{\partial\left(\rho_\mathrm{nf}V^*\right)}{\partial Y}\right] + \alpha\frac{\rho_\mathrm{f} - \rho_\mathrm{num}}{\Delta\tau^2} \tag{27}$$

where α: $(0 \le \alpha \le 1)$ is the relaxation coefficient and ρ_num – the numerical density and it calculated from SPH approximation:

$$\rho_\mathrm{num} = \sum_j m_j W_{ij} \tag{28}$$

where m_j refers to the mass of neighbor particle j, W_{ij} is the kernel function, eq. (36), and i – the target particle.

Hence, the final velocity is calculated:

$$U^{n+1} = U^* - \Delta\tau\left(\frac{\partial P}{\partial X}\right)^{n+1} \tag{29}$$

$$V^{n+1} = V^* - \Delta\tau\left(\frac{\partial P}{\partial Y}\right)^{n+1} \tag{30}$$

The temperature and nanoparticle volume fraction are calculated:

$$\theta^{n+1} = \theta^n + \Delta\tau\frac{\left(\rho C_p\right)_\mathrm{f}}{\left(\rho C_p\right)_\mathrm{nf}}\left[\frac{\partial}{\partial X}\left(\frac{K_\mathrm{nf}}{K_f}\frac{\partial\theta}{\partial X}\right)^n + \frac{\partial}{\partial Y}\left(\frac{K_\mathrm{nf}}{K_\mathrm{f}}\frac{\partial\theta}{\partial Y}\right)^n + \right.$$
$$\left. + \frac{1}{\mathrm{Le}}\left(\left[D_B^*\left(\frac{\partial\varphi^*}{\partial X}\frac{\partial\theta}{\partial X} + \frac{\partial\varphi^*}{\partial Y}\frac{\partial\theta}{\partial Y}\right)\right]^n + \left\{\frac{D_T^*}{N_{BT}}\frac{\left[\left(\frac{\partial\theta}{\partial X}\right)^2 + \left(\frac{\partial\theta}{\partial Y}\right)^2\right]}{1+\frac{\theta}{\delta}}\right\}^n\right)\right] \tag{31}$$

$$\varphi^{*n+1} = \varphi^{*n} + \Delta\tau\left\{\frac{\mathrm{Pr}}{\mathrm{Sc}}\frac{\partial}{\partial X}\left(D_B^*\frac{\partial\varphi^*}{\partial X}\right)^n + \frac{\mathrm{Pr}}{\mathrm{Sc}}\frac{\partial}{\partial Y}\left(D_B^*\frac{\partial\varphi^*}{\partial Y}\right)^n + \right.$$
$$\left. + \frac{\mathrm{Pr}}{\mathrm{Sc}}\frac{\partial}{\partial X}\left[\frac{D_T^*}{N_{BT}\left(1+\frac{\theta}{\delta}\right)}\frac{\partial\theta}{\partial X}\right]^n + \frac{\mathrm{Pr}}{\mathrm{Sc}}\frac{\partial}{\partial Y}\left[\frac{D_T^*}{N_{BT}\left(1+\frac{\theta}{\delta}\right)}\frac{\partial\theta}{\partial Y}\right]^n\right\} \tag{32}$$

The positions of the fluid particles are updated at each time step:

$$X^{n+1} = X^n + \Delta\tau U^{n+1},\ Y^{n+1} = Y^n + \Delta\tau V^{n+1} \tag{33}$$

Shifting technique [50, 51] for preventing the particles disorders:

$$\mathcal{F}_{i'} = \mathcal{F}_i + \left(\nabla\mathcal{F}\right)_i \delta\boldsymbol{r}_{ii'} + \mathcal{O}\left(\delta\boldsymbol{r}_{ii'}^2\right) \tag{34}$$

$$\delta\boldsymbol{r}_{ii'} = -\mathcal{D}\nabla C_i' \tag{35}$$

where $\mathcal{F}$ is the any hydrodynamic function and $\nabla C'_i$ – the gradient of particle concentration.

The ISPH formulation

In the current simulations, a quantic kernel function, W, was used:

$$W\left(q,h\right) = \frac{3}{16\pi h^2}\begin{cases} \left(2-q\right)^5 - 16\left(1-q\right)^5 & 0 \le q \le 1 \\ \left(2-q\right)^5 & 1 < q \le 2 \\ 0 & q > 2 \end{cases} \tag{36}$$

where $q = \boldsymbol{r}_{ij}/h$. In this study, the main concept of SPH approximation using renormalization factor γ_i is expressed:

$$\left\langle f\left(\boldsymbol{r}_i\right)\right\rangle = \frac{1}{\gamma_i}\sum_j^n \frac{m_j}{\rho_j} f\left(\boldsymbol{r}_j\right) W\left(\boldsymbol{r}_{ij}, h\right) \tag{37}$$

The description of renormalization factor γ_i and its first derivative according to [52, 53] are defined:

$$\gamma_i = \int_{\mathrm{U}_i} W\left(\left|\boldsymbol{r}_{ab}\right|\right) \mathrm{d}\Omega\left(\boldsymbol{r}_j\right) \tag{38}$$

$$\nabla\gamma_{ie} = -\int_{e_1}^{e_2} \boldsymbol{n}\left(\boldsymbol{r}_j\right) W\left(\boldsymbol{r}_{ij}\right) \mathrm{d}\Gamma\left(\boldsymbol{r}_j\right) \tag{39}$$

The ISPH discretization of the solving technique, eqs. (25)-(31), has been discussed in details during our previous studies [52-54].

Treatment of boundary particles in ISPH method

In this study, the kernel renormalization function was adopted for the wall boundary treatment. This boundary treatment was introduced and validated for several applications by Nguyen *et al.* [52-54]. In renormalization wall boundary treatment, no need for extra dummy particles around the boundary wall as seen in fig. 2. Another advantage of this treatment appears in applying Neumann boundary conditions without any special treatment as it appears directly in ISPH discretization. Figure 2(a) shows the schematic diagram of the renormalization wall boundary. Here, combined kernel renormalization function, γ_i, with the impact of boundary particles were used for treating renormalization wall boundary. In addition, Figure 2(b) shows the initial schematic diagram of dummy wall boundary particles. The dummy wall boundary considers an efficient way to treat the rigid wall boundary. The several layers of dummy boundary particles reduce the error of truncated kernel function.

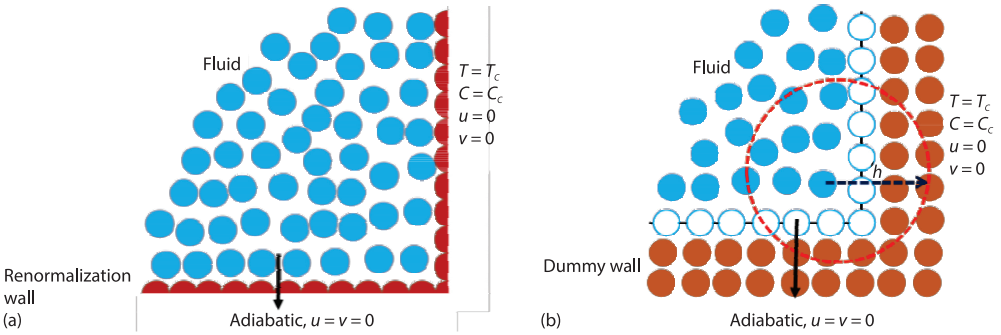

Figure 2. Schematic diagram of (a) renormalization wall boundary and (b) dummy wall boundary

Results and discussion

Figure 3 shows the valuable comparisons for the implementation of the conditions of the nanoparticles volume fraction. The test consists of the streamlines, isotherms and nanoparticles volume fraction obtained in this study and those of Corcione *et al*. [19] at Ra = $3.37 \cdot 10^5$ and $\phi = 0.04$. It is found that the results show excellent agreements with the previous published results.

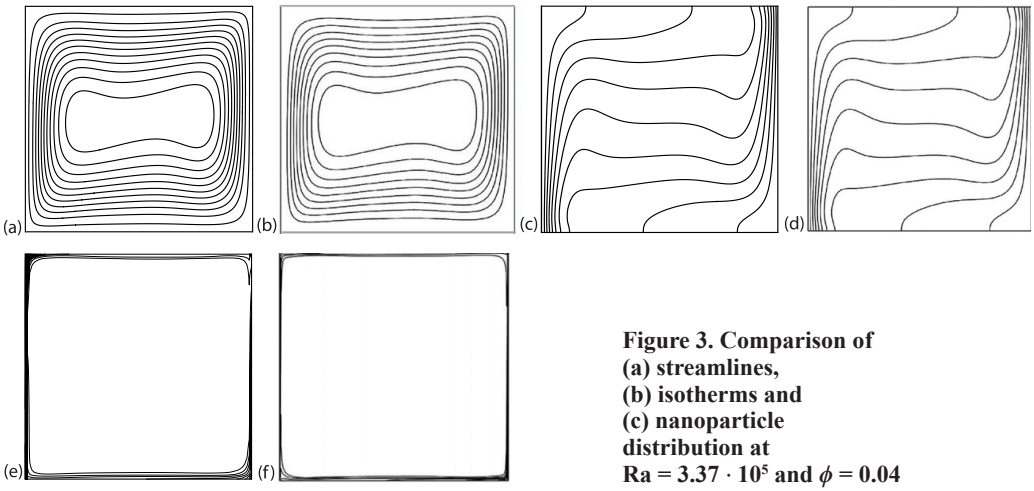

Figure 3. Comparison of (a) streamlines, (b) isotherms and (c) nanoparticle distribution at Ra = $3.37 \cdot 10^5$ and $\phi = 0.04$

In fig. 4, impacts of the *T*-shaped pipe lengths $L_b = 0.2, 0.4, 0.5, 0.6$ on the isotherms contours are illustrated. There is an isothermal zone is noted around the inner shaped while the less-temperature zones occur near the vertical walls. In addition, the increase in lengths of the *T*-shaped pipe causes an extra heat generation inside the geometry and hence distributions of the temperature inside the flow domain are supported. In the same context, fig. 5 shows the influences of the *T*-pipe length ($L_b = 0.2, 0.4, 0.5, 0.6$) on the streamlines contours at Ra = 10^4, $W_b = 0.08$, $W_t = 0.06$, and $\phi_{avg} = 0.03$. Here, it should be mentioned that the increase in lengths of the *T*-shaped pipe causes that the geometry be complicated and consequently the nanofluid-flow is seen inactive, particularly, at the top part of the domain. Also, it is observed that the nanofluid-flow is decreased when L_b is growing from 0.2-0.4, however, more increase in L_b causes that the nanofluid-flow is concentrated at the lower part of the enclosure with an increase in the maximum values of the stream function.

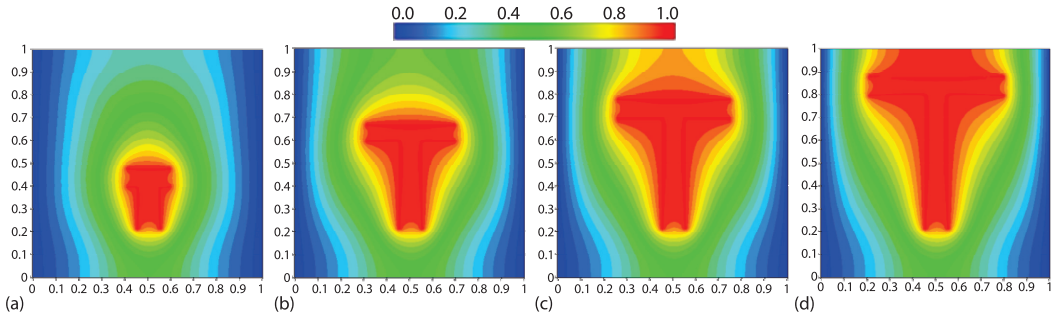

Figure 4. Impacts of *T*-pipe length (L_b = 0.2, 0.4, 0.5, 0.6) on the isothermal contours at Ra = 10^4, W_b = 0.08, W_t = 0.06, and ϕ_{avg} = 0.03; (a) L_b = 0.2, (b) L_b = 0.4, (c) L_b = 0.5, and (d) L_b = 0.6

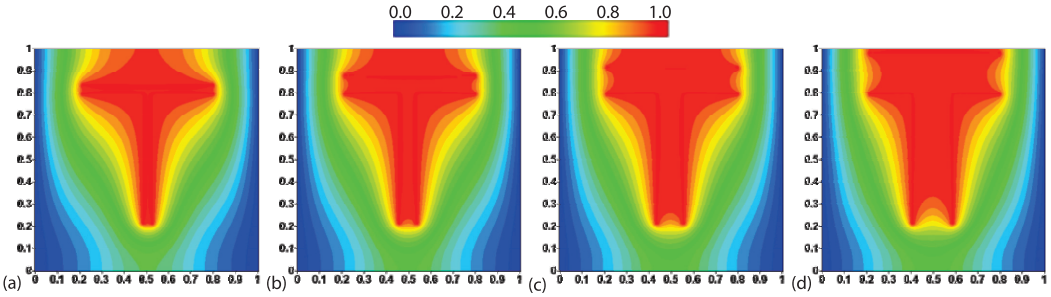

Figure 5. Impacts of *T*-pipe length (L_b = 0.2, 0.4, 0.5, 0.6) on the streamlines contours at Ra = 10^4, W_b = 0.08, W_t = 0.06, and ϕ_{avg} = 0.03; (a) L_b = 0.2 ($|\psi|_{max}$ = 0.342), (b) L_b = 0.4 ($|\psi|_{max}$ = 0.287), (c) L_b = 0.5 ($|\psi|_{max}$ = 0.305), and (d) L_b = 0.6 ($|\psi|_{max}$ = 0.326)

Figure 6 displays the streamlines contours for variations of the *T*-pipe width $W_b = W_t$ = 2, 6, 10, 16 cm at Ra = 10^4. During these computations, value of ϕ_{avg} is fixed at 0.03. The figure disclosed that the thermal zone along the inner shape is enhanced as the width of the *T*-pipe channels are enhanced due to the increase in the temperature generation inside the flow domain. Additionally, distributions of the nanofluid temperature as well as the thermal boundary-layers along the vertical walls are supported as W_b and W_t are varied. On the other hand, fig. 7 reveals that the low values of width of the *T*-pipe mean that the *T*-pipe channels are narrow therefore, in this case the nanofluid-flow is seen to be weak, particularly, at the top part of the enclosure. However, as width of the *T*-pipe channels are increased, the nanofluid inters inside the channels and hence there are streamlines are seen at the upper part of the do-

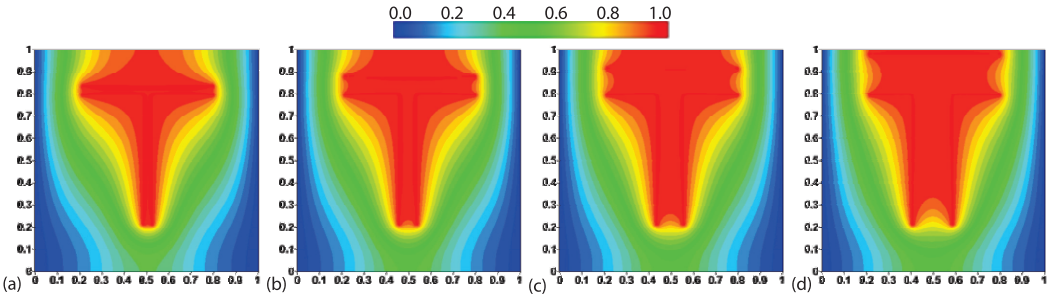

Figure 6. Impacts of *T*-pipe width ($W_b = W_t$ = 2, 6, 10, 16) on the isothermal contours at Ra = 10^4, L_b = 0.6, and ϕ_{avg} = 0.03; (a) $W_b = W_t$ = 2 cm, (b) $W_b = W_t$ = 6 cm, (c) $W_b = W_t$ = 10 cm, and (d) $W_b = W_t$ = 16 cm

main. In the same context, the higher value of the stream function, ($|\psi|_{max}$ = 0.356), is noted at $W_b = W_t$ = 2 cm while it's low value is ($|\psi|_{max}$ = 0.325) and it is noted at $W_b = W_t$ = 10 cm.

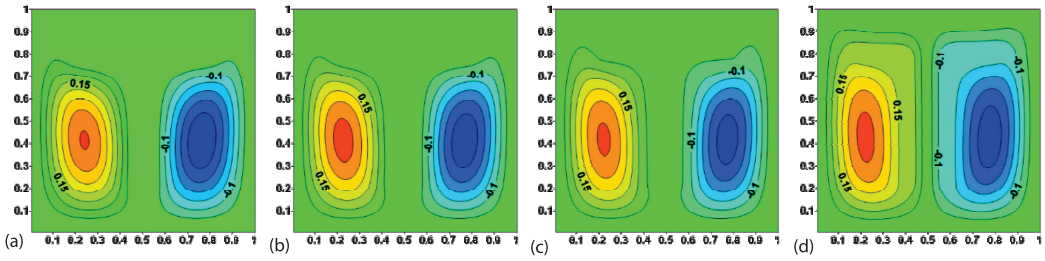

Figure 7. Impacts of *T*-pipe width ($W_b = W_t$ = 2, 6, 10, 16) on the streamlines isothermal contours at Ra = 10^4, L_b = 0.6, and ϕ_{avg} = 0.03; (a) $W_b = W_t$ = 2 cm ($|\psi|_{max}$ = 0.356), (b) $W_b = W_t$ = 6 cm ($|\psi|_{max}$ = 0.337), (c) $W_b = W_t$ = 10 cm ($|\psi|_{max}$ = 0.325), and (d) $W_b = W_t$ = 16 cm ($|\psi|_{max}$ = 0.331)

In fig. 8, impacts of the nanoparticles volume fraction on the isothermal contours at Ra = 10^4, L_b = 0.6, W_b = 0.08, and W_t = 0.06 are checked. The results demonstrated that the increase in the average values of the nanoparticles volume fraction ϕ_{avg} enhanced the thermal conductivity of the liquid and thus the thermal boundary-layers near the inner shape and along the vertical walls are increased. Figure 9 displays effects of average of the nanoparticles volume fraction ϕ_{avg} on distributions of the normalized nanoparticle volume fractions ϕ^* at Ra = 10^4, W_b = 0.08 and W_t = 0.06. Based on the inverse relation between ϕ_{avg} and ϕ^*, it is clear that the increase in ϕ_{avg} causes a reduction in distributions of ϕ^*. Also, it is seen that there are contours

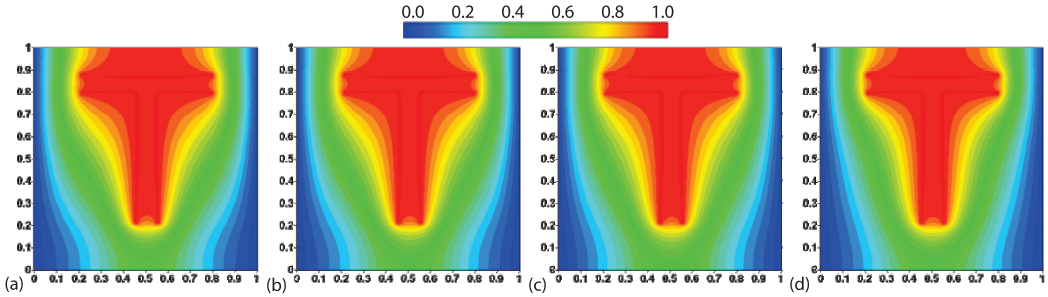

Figure 8. Impacts of the average value of the nanoparticles volume fractions (ϕ_{avg} = 0.01, 0.03, 0.05, 0.1) on the isothermal contours at Ra = 10^4, L_b = 0.6, W_b = 0.08, and W_t = 0.06; (a) ϕ_{avg} = 0.01, (b) ϕ_{avg} = 0.03, (c) ϕ_{avg} = 0.05, and (d) ϕ_{avg} = 0.1

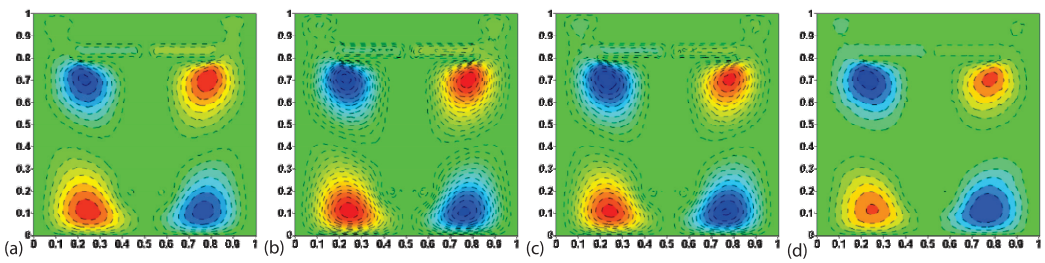

Figure 9. Impacts of average value of nanoparticles volume fractions (ϕ_{avg} = 0.01, 0.03, 0.05, 0.1) on nanoparticles volume fraction contours Ra = 10^4, L_b = 0.6, W_b = 0.08, and W_t = 0.06; (a) ϕ_{avg} = 0.01, (b) ϕ_{avg} = 0.03, (c) ϕ_{avg} = 0.05, and (d) ϕ_{avg} = 0.1

of ϕ^* inside the horizontal channel of the T-pipe and this is due to loading the nanoparticles by the fluid during the flow. However, the viscosity of the mixture is enhanced as ϕ_{avg} is varied from 0.01-0.1 and consequently there is a deactivation in the nanofluid-flow is observed as ϕ_{avg} increases. This behavior is presented, clearly, in fig. 10. In this figure the maximum values of the stream function is reduced by 80.8% when ϕ_{avg} is varied from 1-10%.

In this study, the $\overline{Nu}$ are calculated along the inner *T*-pipe and at the left wall of the enclosure. Behaviors of this coefficient under effects of the controlling parameters, namely, lengths of the *T*-pipe channels L_b, width of the *T*-pipe channels W_b and W_t and the average values of the nanoparticles volume fraction are presented in figs. 11-13. Figure 11 shows that the $\overline{Nu}$ along the inner shape boundaries is reduced as L_b is increased while the increase in L_b causes that the temperature gradients near the vertical walls are enhanced and thus the $\overline{Nu}$ is increased due to the increase in the temperature differences. Also, fig. 12 reveals an enhancement in the $\overline{Nu}$ along the inner shape and at the left wall as width of the *T*-pipe is increased due to the support in the thermal boundary-layers along the domain boundaries. In the same context, fig. 13 shows that the increase in the average values of the nanoparticles volume fraction results in an enhancement in the thermal conductivity of the liquid and consequently the $\overline{Nu}$ at either the inner boundaries or the outer boundaries is increased as ϕ_{avg} is growing.

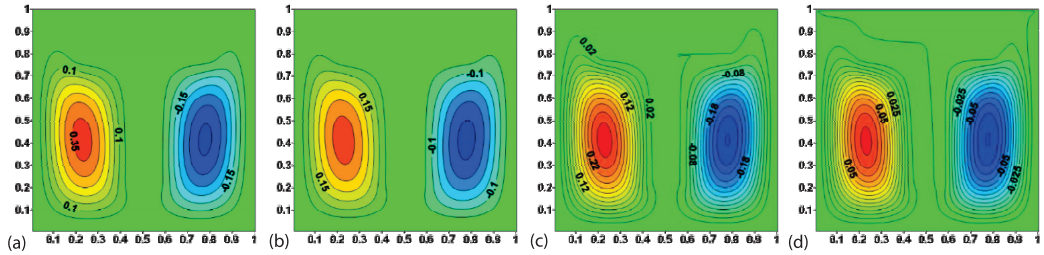

Figure 10. Impacts of the average value of the nanoparticles volume fractions (ϕ_{avg} = 0.01, 0.03, 0.05, 0.1) on the streamlines contours Ra = 10^4, L_b = 0.6, W_b = 0.08, and W_t = 0.06; (a) ϕ_{avg} = 0.01 ($|\psi|_{max}$ = 0.375), (b) ϕ_{avg} = 0.03 ($|\psi|_{max}$ = 0.327), (c) ϕ_{avg} = 0.05 ($|\psi|_{max}$ = 0.271), and (d) ϕ_{avg} = 0.1 ($|\psi|_{max}$ = 0.072)

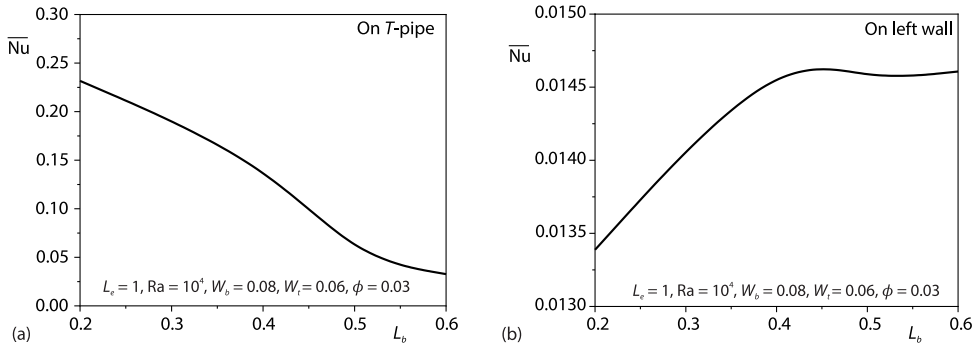

Figure 11. The $\overline{Nu}$ on *T*-pipe and left cavity wall under the impacts of *T*-pipe length (Lb = 0.2, 0.4, 0.5, 0.6) at Ra = 104, Wb = 0.08, Wt = 0.06, and ϕavg = 0.03; (a) on *T*-pipe and (b) on left cavity wall

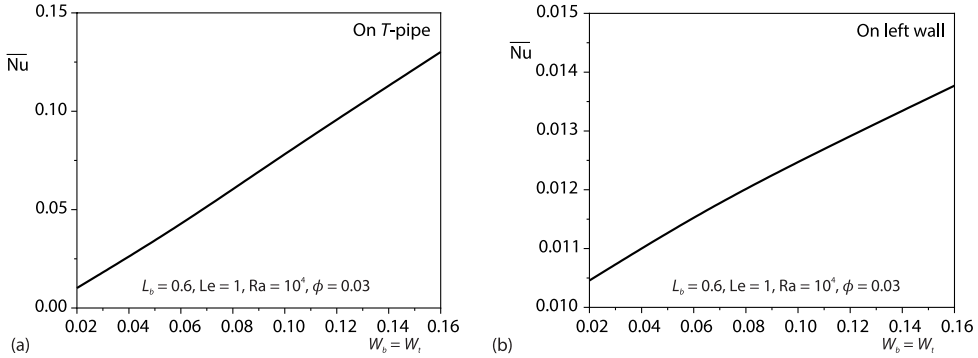

Figure 12. The $\overline{Nu}$ on *T*-pipe and left cavity wall under the impacts of *T*-pipe width ($W_b = W_t = 0.2, 0.4, 0.5, 0.6$) at Ra = 10^4, and $\phi_{avg} = 0.03$; (a) on *T*-pipe and (b) on left cavity wall

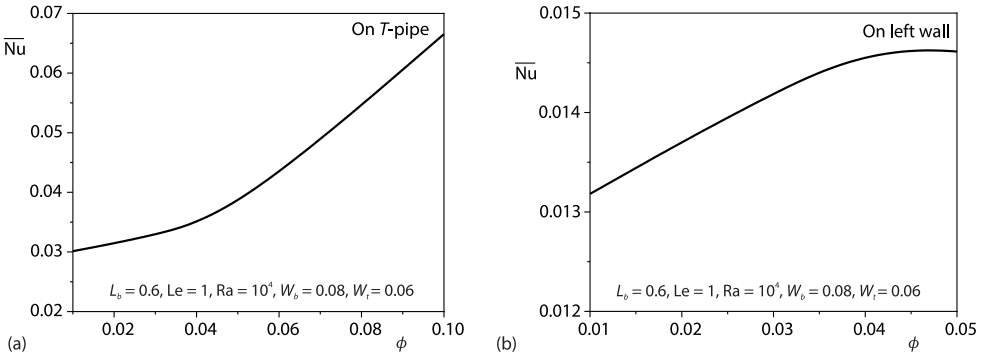

Figure 13. The $\overline{Nu}$ on *T*-pipe and left cavity wall under the impacts of *T*-pipe width ($W_b = W_t = 0.2, 0.4, 0.5, 0.6$) at Ra = 10^4, and $\phi_{avg} = 0.03$; (a) on *T*-pipe and (b) on left cavity wall

Conclusions

Numerical study based on the incompressible SPH method has been conducted for the nanofluid and thermal fields within enclosures containing open *T*-shaped pipes and are filled by Al_2O_3-H_2O nanomixture. The non-homogenous Buongiorno's two-phase model is applied to simulate the nanofluid transport. Non-fixed lengths and widths for the inner *T*-pipe were considered while the thermophysical properties of the nanofluid were assumed to be functions in diameters of the base fluid and nanoparticles molecules. During the investigation of this physical situation, the following main results are summarized:

- An increase in lengths of the *T*-pipe channels enhances the temperature distributions as well as the $\overline{Nu}$ at the left wall.
- Distributions of the nanofluid temperature, the $\overline{Nu}$ along the inner boundaries and the $\overline{Nu}$ at the left wall are supported as widths of the *T*-pipe channels is increased
- The increase in the average values of the nanoparticles volume fraction causes an enhancement in the thermal boundary-layers while a deactivation in the nanofluid-flow is noted
- Both the $\overline{Nu}$ along the inner boundaries and at the left wall are boosted when the average values of the nanoparticles volume fraction is growing.

Acknowledgment

The authors extend their appreciation the Deanship of Scientific Research at King Khalid University for funding this work through research groups program under Grant No. (R.G.P1/27/42).

Nomenclature

C_p – specific heat capacity, [Jkg^{-1}K^{-1}]
D_B – Brownian diffusion coefficient
D_T – thermophoresis coefficient
d_f, d_p – diameters of H_2O and Al_2O_3 molecules
g – gravity acceleration, [ms^{-2}]
K_B – Boltzmann's constant, [JK^{-1}]
k – thermal conductivity, [Wm^{-1}K^{-1}]
L – size of the cavity, [m]
Le – Lewis number
N_{BT} – diffusivity ratio parameter
Nu – Local Nusselt number
$\overline{\text{Nu}}$ – average Nusselt number
p – pressure, [Nm^{-2}]
Pr – Prandtl number
Ra – Rayleigh number
Sc – Schmidt number
T – temperature, [K]
t – time, [s]
U, V – dimensionless velocity components
u_B – Brownian velocity
u, v – elocity components in the x- and y-direction, [ms^{-1}]
X, Y – dimensionless Cartesian co-ordinates
x, y – dimensional Cartesian co-ordinates, [m]

Greek symbols

α – thermal diffusivity, [m^{2}s^{-1}]
β – coefficient of thermal expansion, [K^{-1}]
γ – heat capacity ratio
θ – dimensionless temperature
μ – dynamic viscosity, [kgm^{-1}s^{-1}]
ν – kinematic viscosity, [m^{2}s^{-1}]
ρ – density, [kgm^{-3}]
τ – dimensionless time
φ^* – dimensionless nanoparticle volume fraction
ϕ – solid volume fraction

Subscripts

nf – effective
f – fluid
fr – freezing
p – porous medium
h – hot
c – cold

References

[1] Muhammad, M. A., *et al*., The Use of Nanofluids for Enhancing the Thermal Performance of Stationary Solar Collectors: A Review, *Renewable and Sustainable Energy Reviews*, *63* (2016), Sept., pp. 226-236
[2] Xu, H. J., *et al*., Review on Heat Conduction, Heat Convection, Thermal Radiation and Phase Change Heat Transfer of Nanofluids in Porous Media: Fundamentals and Applications, *Chemical Engineering Science*, *195* (2019), Feb., pp. 462-483
[3] Mahian, O., *et al*., A Review of the Applications of Nanofluids in Solar Energy, *International Journal of Heat and Mass Transfer*, *57* (2013), 2, pp. 582-594
[4] Khanafer, K., Vafai, K., A Review on the Applications of Nanofluids in Solar Energy Field, *Renewable Energy*, *123* (2018), Aug., pp. 398-406
[5] Elsheikh, A., *et al*., Applications of Nanofluids in Solar Energy: A Review of Recent Advances, *Renewable and Sustainable Energy Reviews*, *82* (2018), Part 3, pp. 3483-3502
[6] Hajmohammadi, M. R., Assessment of a Lubricant Based Nanofluid Application in a Rotary System, *Energy Conversion and Management, 146* (2017), Aug., pp. 78-86
[7] Rashidi, S., *et al*., Applications of Nanofluids in Condensing and Evaporating Systems, *Journal of Thermal Analysis and Calorimetry*, *131* (2018), 3, pp. 2027-2039
[8] Mahian, O., *et al*., Recent Advances in Modelling and Simulation of Nanofluid-Flows – Part II: Applications, *Physics Reports*, *791* (2019), Feb., pp. 1-59
[9] Rashidi, S., *et al*., Combination of Nanofluid and Inserts for Heat Transfer Enhancement, *Journal of Thermal Analysis and Calorimetry*, *135* (2019), Feb., pp. 437-460
[10] Jayhooni, S. M. H., Rahimpour, M. R., Effect of Different Types of Nanofluids on Free Convection Heat Transfer around Spherical Mini-Reactor, *Superlattices and Microstructures*, *58* (2013), June, pp. 205-217
[11] Jmai, R., *et al*., Heat Transfer and Fluid-Flow of Nanofluid-Filled Enclosure with Two Partially Heated Side Walls and Different Nanoparticles, *Superlattices and Microstructures*, *53* (2013), 1, pp. 130-154
[12] Sameh E. A., *et al*., Magnetohydrodynamic Convective Flow of Nanofluid in Double Lid-Driven Cavities under Slip Conditions, *Thermal Science*, *25* (2021), 3A, pp. 1703-1717

[13] Zeinab Z. R., *et al*., Heat Transfer Enhancement in the Complex Geometries Filled with Porous Media, *Thermal Science*, *25* (2021), 1A, pp. 39-57
[14] Ahmed, S. E., *et al*., Magnetohydrodynamic Mixed Thermo-Bioconvection in Porous Cavity Filled by Oxytactic Microorganisms, *Thermal Science*, *22* (2018), 6B, pp. 2711-2721
[15] Wen, D., Ding, Y., Experimental Investigation into Convective Heat Transfer of Nanofluids at the Entrance Region under Laminar Flow Conditions, *International Journal of Heat and Mass Transfer*, *47* (2004), 24, pp. 5181-5188
[16] He, Y., *et al*., Numerical Investigation into the Convective Heat Transfer of TiO_2 Nanofluids Flowing through a Straight Tube under the Laminar Flow Conditions, *Applied Thermal Engineering*, *29* (2009), 10, pp. 1965-1972
[17] Moghari, R. M., *et al*., Two-Phase Mixed Convection Al_2O_3-Water Nanofluid-Flow in an Annulus, *International Journal of Multi-phase Flow*, *37* (2011), 6, pp. 585-595
[18] Buongiorno, J., Convective Transport in Nanofluids, *Journal of Heat Transfer*, *128* (2005), 3, pp. 240-250
[19] Corcione, M., *et al*., Two-Phase Mixture Modelling of Natural-Convection of Nanofluids with Temperature-Dependent Properties, *International Journal of Thermal Sciences*, *71* (2013), Sept., pp. 182-195
[20] Corcione, M., *et al*., A Two-Phase Numerical Study of Buoyancy-Driven Convection of Alumina-Water Nanofluids in Differentially-Heated Horizontal Annuli, *International Journal of Heat and Mass Transfer*, *65* (2013), Oct., pp. 327-338
[21] Saghir, M. Z., *et al*., Two-Phase and Single Phase Models of Flow of Nanofluid in a Square Cavity: Comparison with Experimental Results, *International Journal of Thermal Sciences*, *100* (2016), Feb., pp. 372-380
[22] Kakac, S., Pramuanjaroenkij, A., Single-Phase and Two-Phase Treatments of Convective Heat Transfer Enhancement with Nanofluids – A State-of-the-Art Review, *International Journal of Thermal Sciences*, *100* (2016), Feb., pp. 75-97
[23] Sheikholeslami, M., *et al*., Two-Phase Simulation of Nanofluid-Flow and Heat Transfer Using Heatline Analysis, *International Communications in Heat and Mass Transfer*, *47* (2013), Oct., pp. 73-81
[24] Garoosi, F., *et al*., Numerical Simulation of Natural-Convection and Mixed Convection of the Nanofluid in a Square Cavity Using Buongiorno Model, *Powder Technology*, *268* (2014), Dec., pp. 279-292
[25] Sheremet, M. A., *et al*., The 3-D Natural-Convection in a Porous Enclosure Filled with a Nanofluid Using Buongiorno's Mathematical Model, *International Journal of Heat and Mass Transfer*, *82* (2015), Mar., pp. 396-405
[26] Sheremet, M. A., Pop, I., Mixed Convection in a Lid-Driven Square Cavity Filled by a Nanofluid: Buongiorno's Mathematical Model, *Applied Mathematics and Computation*, *266* (2015), Sept., pp. 792-808
[27] Dogonchi, A. S., *et al*., Analytical Solution and Heat Transfer of Two-Phase Nanofluid-Flow between Non-Parallel Walls Considering Joule Heating Effect, *PTEC Powder Technology*, *318* (2017), Aug., pp. 390-400
[28] Dogonchi, A. S., *et al*., Free Convection of Copper-Water Nanofluid in a Porous Gap between Hot Rectangular Cylinder and Cold Circular Cylinder under the Effect of Inclined Magnetic Field, *Journal Therm Anal Calorim Journal of Thermal Analysis and Calorimetry: An International Forum for Thermal Studies*, *135* (2019), 2, pp. 1171-1184
[29] Dogonchi, A. S., *et al*., A numerical Investigation of Magneto-Hydrodynamic Natural-Convection of Cu-Water Nanofluid in a Wavy Cavity Using CVFEM, *Journal of Thermal Analysis and Calorimetry: An International Forum for Thermal Studies*, *135* (2019), 4, pp. 2599-2611
[30] Rehman, K. U., *et al*., Heat Transfer Individualities Due to Evenly Heated T-Shaped Blade Rooted in Trapezium Enclosure: Numerical Analysis, *Case Studies in Thermal Engineering*, *22* (2020), 100778
[31] Sheikhzadeh, G. A., *et al*., Effects of Nanoparticles Transport Mechanisms on Al_2O_3-Water Nanofluid Natural-Convection in a Square Enclosure, *International Journal of Thermal Sciences*, *66* (2013), Apr., pp. 51-62
[32] Motlagh, S. Y., Soltanipour, H., Natural-Convection of Al_2O_3-Water Nanofluid in an Inclined Cavity Using Buongiorno's Two-Phase Model, *International Journal of Thermal Sciences*, *111* (2017), Jan., pp. 310-320
[33] Motlagh, S. Y., *et al*., Two-Phase Modelling of the Free Convection of Nanofluid Inside the Inclined Porous Semi-Annulus Enclosure, *International Journal of Mechanical Sciences*, *164* (2019), 105183
[34] Gingold, R. A., *et al*., Smoothed Particle Hydrodynamics: Theory and Application Non-Spherical Stars, Monthly Notices of the Royal Astronomical Society, *181* (1977), 3, pp. 375-389
[35] Lucy, L. B., A Numerical Approach to the Testing of the Fission Hypothesis, *The Astronomical Journal*, *82* (1977), Dec., pp. 1013-1024

[36] Monaghan, J. J., Particle Methods for Hydrodynamics, *Computer Physics Reports*, *3* (1985), 2, pp. 71-124
[37] Aly, A. M., Modelling of Multi-Phase Flows and Natural-Convection in a Square Cavity Using an Incompressible Smoothed Particle Hydrodynamics, *International Journal of Numerical Methods for Heat & Fluid-Flow*, *25* (2015), 3, pp. 513-533
[38] Dalrymple, R. A., Rogers, B., Numerical Modelling of Water Waves with the SPH Method, *Coastal Engineering*, *53* (2006), 2-3, pp. 141-147
[39] Hu, X. Y., Adams, N. A., A Multi-Phase SPH Method for Macroscopic and Mesoscopic Flows, *Journal of Computational Physics*, *213* (2006), 2, pp. 844-861
[40] Kulasegaram, S., *et al*., High Pressure Die Casting Simulation Using a Lagrangian Particle Method, *Communications in Numerical Methods in Engineering*, *19* (2003), 9, pp. 679-687
[41] Koukouvinis, P. K., *et al*., An Improved MUSCL Treatment for the SPH-ALE Method: Comparison with the Standard SPH Method for the Jet Impingement Case, *International Journal for Numerical Methods in Fluids*, *71* (2013), 9, pp. 1152-1177
[42] Ferrand, M., *et al*., Unified Semi-Analytical Wall Boundary Conditions for Inviscid, Laminar or Turbulent Flows in the Meshless SPH Method, *International Journal for Numerical Methods in Fluids*, *71* (2013) 4, pp. 446-472
[43] Danis, M., *et al*., The ISPH Modelling of Transient Natural-Convection, *International Journal of Computational Fluid Dynamics*, *27* (2013), 1, pp. 15-31
[44] Aly, A. M., Raizah, Z., Incompressible Smoothed Particle Hydrodynamics (ISPH) Method for Natural-Convection in a Nanofluid-Filled Cavity Including Rotating Solid Structures, *International Journal of Mechanical Sciences*, *146* (2018), Aug., pp. 125-140
[45] Aly, A. M., Asai, M., Water Entry of Decelerating Spheres Simulations Using Improved ISPH Method, *Journal of Hydrodynamics*, *30* (2018), 1, pp. 1120-1133
[46] Ahmed, S. E., Aly, A. M., Natural-Convection in a Nanofluid-Filled Cavity with Solid Particles in an Inner Cross Shape Using ISPH Method, *International Journal of Heat and Mass Transfer*, *141*, (2019) July, pp. 390-406
[47] Aly, A. M., Raizah, Z. A. S., Incompressible Smoothed Particle Hydrodynamics Simulation of Natural-Convection in a Nanofluid-Filled Complex Wavy Porous Cavity with Inner Solid Particles, Physica A: *Statistical Mechanics and its Applications*, *537* (2020), 122623
[48] Corcione, M., Empirical Correlating Equations for Predicting the Effective Thermal Conductivity and Dynamic Viscosity of Nanofluids, *Energy Convers Manag*, 52 (2011), 1, pp. 789-93
[49] Cummins, S. J., Rudman, M., An SPH Projection Method, *Journal of Computational Physics*, *152* (1999), 2, pp. 584-607
[50] Lind, S. J., *et al*., Incompressible Smoothed Particle Hydrodynamics for Free-Surface Flows: A Generalised Diffusion-Based Algorithm for Stability and Validations for Impulsive Flows and Propagating Waves, *Journal of Computational Physics*, *231* (2012), 4, pp. 1499-1523
[51] Skillen, A., *et al*., Incompressible Smoothed Particle Hydrodynamics (SPH) with Reduced Temporal Noise and Generalised Fickian Smoothing Applied to Body-Water Slam and Efficient Wave-Body Interaction, *Computer Methods in Applied Mechanics and Engineering*, *265* (2013), Oct., pp. 163-173
[52] Nguyen, M. T., *et al*., Effect of a Wavy Interface on the Natural-Convection of a Nanofluid in a Cavity with a Partially Layered Porous Medium Using the ISPH Method, *Numerical Heat Transfer* – Part A: *Applications*, *72* (2017), 1, pp. 68-88
[53] Nguyen, M. T., *et al*., Improved Wall Boundary Conditions in the Incompressible Smoothed Particle Hydrodynamics Method, *International Journal of Numerical Methods for Heat & Fluid-Flow*, *28* (2018) 3, pp. 704-725
[54] Nguyen, M. T., *et al*., The ISPH Modelling of Natural-Convection Heat Transfer with an Analytical Kernel Renormalization Factor, *Meccanica*, *53* (2018), Jan., pp. 2299-2318

Paper submitted: November 22, 2020
Paper revised: February 18, 2021
Paper accepted: February 23, 2021